Applied Energy 346 (2023) 121357

Contents lists available at ScienceDirect

Applied Energy

journal homepage: www.elsevier.com/locate/apenergy

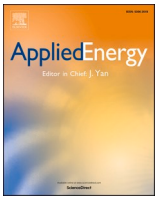

Energy efficiency assessment of hydrogen recirculation ejectors for proton exchange membrane fuel cell (PEMFC) system

Hongbing Ding [a], Yuanyuan Dong [a], Yu Zhang [a], Yan Yang [b,*], Chuang Wen [b,*]

[a] Tianjin Key Laboratory of Process Measurement and Control, School of Electrical and Information Engineering, Tianjin University, Tianjin 300072, China
[b] Faculty of Environment, Science and Economy, University of Exeter, Exeter EX4 4QF, United Kingdom

HIGHLIGHTS

- Propose a mathematical model integrating non-equilibrium condensation and entropy generation.
- Wet gas model had a good prediction ability for ejectors with an MRE of 2.53%
- The condensation strength in the ejector increased with the rise of the primary pressure
- The dry gas model overestimated the entropy with 138.66 J kg^{-1} K^{-1} at the primary pressure of 5.0 bar
- The dry gas model overestimated the maximum exergy destruction and exergy destruction ratio of 41.83 kJ/kg and 15.83%

ARTICLE INFO

Keywords:
Hydrogen
PEMFC
Ejector
Exergy destruction
Non-equilibrium condensation
Proton exchange membrane fuel cell

ABSTRACT

The ejector is the core component for hydrogen recirculation in a proton exchange membrane fuel cell (PEMFC) system. However, in the past, the computational fluid dynamics (CFD) simulation of the ejector mainly focused on the influence of the change of the structural parameters on its performance, while the research on phase change condensation was lacking. Here, we proposed a two-phase flow model integrating the non-equilibrium phase change conservation equations and four categories of entropy transport equations, which analysed the phase change characteristics and the influence of different primary pressures on the property of ejector and internal entropy and exergy under the dry and wet gas models. We validated that the wet gas model has a good prediction ability with an MRE of only 2.53%. There was a significant difference between the dry and wet gas models, for example, the dry gas model predicted a larger Mach number and entrainment ratio, while the temperature and pressure were less than that of the wet gas model. Finally, the entropy and exergy were analysed, and the dry gas model overestimated the entropy generation, i.e, when the pressure of the primary inlet raised to 5.0 bar, the entropy generation overestimated by the dry gas model had reached 138.66 J $kg^{-1}K^{-1}$. The exergy destruction and exergy destruction ratio both increased with the rise of primary pressure. The dry gas model overestimated the exergy destruction and exergy destruction ratio, and the maximum overestimated values can reach 41.83 kJ/kg and 15.83%, respectively.

1. Introduction

In recent years, with the increase in energy consumption and pollutant emissions, environmental problems are becoming more and more prominent, which cannot be underestimated [1]. The development and utilization of clean energy is the key to the overall decarbonization of the world. In other words, without clean energy, decarbonization of transportation [2], buildings, infrastructure [3] as well as industry is difficult to achieve and achieving energy decarbonization is necessary for net zero emissions [4]. Besides, promoting sustainable development [5] and accelerating the realization of carbon peak and carbon neutrality goals have become one of the core strategies of all countries. Therefore, renewable energy [6] and hydrogen fuel production [7] are effective solutions and are also a key part of improving climate change and the energy crisis. At present, hydrogen fuel [8], as recognized as green energy, is the cornerstone of energy transformation with its characteristics of green, zero-carbon, high-density, renewable and storable, and is becoming one of the ideal alternative energy sources [9]. That is, the safe and efficient development and utilization of hydrogen

* Corresponding authors.
E-mail addresses: yanyang2021@outlook.com, y.yang7@exeter.ac.uk (Y. Yang), c.wen@exeter.ac.uk (C. Wen).

https://doi.org/10.1016/j.apenergy.2023.121357
Received 25 February 2023; Received in revised form 5 May 2023; Accepted 25 May 2023

Nomenclature

Term

c_p	specific heat capacity, J $kg^{-1}K^{-1}$
F_s	safety factor, -
h_{lg}	latent heat of water vapour, J kg^{-1}
v_0	correction factor, -
I	nucleation rate, $m^{-3}s^{-1}$
k_B	Boltzmann's constant, 1.38×10^{-23}J K^{-1}
Kn	Knudsen number, –
s	entropy generation, J·kg^{-1}·K^{-1}
M_m	single molecular mass, kg
m_v	liquid mass changing rate, kg $m^{-3}s^{-1}$
N	number of droplets per volume, m^{-3}
N_A	Avogadro number, 6.022×10^{23} /mol
p	pressure, Pa
Pr	Prandtl number, –
q_c	condensation coefficient, -
r	droplet radius, m
r_c	critical radius, m
T_g	fluid temperature, K
V	volume, m^3
Y	liquid fraction, %

Greek

α	droplet growth correction coefficient, -
β	droplet growth correction coefficient, -
γ	specific heat capacity ratio, -
ε	relative error of grids, -
λ	thermal conductivity, W $m^{-1}K^{-1}$
ρ	density of fluid, kg m^{-3}
σ	surface tension, N/m

Subscripts

c	critical
g	gas
l	liquid
s	saturation

energy [10] have become quite necessary. It is noteworthy that a proton exchange membrane fuel cell (PEMFC) [11,12], with high hydrogen energy efficiency, has become the research object of many experts and has shown great advantages. In recent years, great progress has been made in this area. Compared with traditional fuel cells, PEMFC is considered as an ideal battery equipment because of its superior working characteristics and zero pollution [13-16]. The emergence and application of hydrogen recirculation ejectors seem to provide new thought for solving the problem of low energy efficiency in industrial production and contribute feasible solutions to energy conservation. The hydrogen recirculation ejector is the core device of the PEMFC system. Naturally, the performance of the ejector is positively related to the efficiency of the PEMFC system. Up to now, due to the advantages of non-parasitic power, simple structure, high durability [17,18] and easy starting [19,20], the ejector [21] has gradually replaced the mechanical pump and become a very promising component in the high-power PEMFC system [22]. Therefore, more researchers are trying to find its optimal structure and working conditions to make the ejector work in the most advantageous conditions and obtain a higher ability to recover low-level energy.

As an environmentally friendly component, it is expected to recover some low-grade waste heat or renewable energy sources using the ejector, thus contributing to energy conservation in many industrial systems. In addition, the ejector has more superiorities that many other devices cannot replicate [23]. Therefore, the ejector was once considered an ideal energy-saving mechanical device and it has been widely used. Obviously, due to its inherent advantages, many scholars have carried out more in-depth research on ejectors used in PEMFC systems [20] or other high-performance fuel cell systems in recent years. However, it needs to be pointed out that the safety hazards of hydrogen in the storage and transportation process, the high cost of fuel cell development and performance testing system, including the elaborate operation mechanism both in the system itself and ejector, have brought great difficulties to the design and production of ejectors. Therefore, the research on ejectors is mostly based on CFD simulation [24]. Back in 2008, Kim et al. [25] proposed an anode recirculation system using an ejector based on humidified hydrogen and validated the results with the experiments. The proposed design method is not limited by the ejector capacity and working conditions and has many advantages. In 2014, Maghsoodi et al. [26] promoted the geometric parameters of the hydrogen recirculation ejector by using the CFD model. It is found that the optimal NXP increases with the increase of mainstream pressure. And the change in mixing tube length can make the entrainment rate change as high as 27%. In the same year, Hosseinzadeh et al. [27] created a CFD solution to the ejector and aimed at exploring the differences between the traditional single ejector and the dual ejector. The results showed that the performance of a single injector is difficult to meet the scope of work in fuel cell systems. Yin [28] conducted a numerical investigation on the impact of pipe arguments on ejector internal characteristics. Liu et al. [29] conducted a three-dimensional model and numerical simulation of the ejector in the fuel cell system under 130 kW operating power and analysed the influence of primary flow operating pressure, relative humidity and nitrogen content on the condensation intensity inside the ejector from multiple perspectives. Yang et al. [30] established a CFD hydrogen recirculation system model taking into account the pressure drops characteristics and verified the impact of the injector geometric arguments and external factors of simulation on its characteristics.

In conclusion, the above research was focused on the reform of the ejector structure itself and the overall design. However, in the actual production process, the PEMFC system will operate under complex and changeable working conditions. More importantly, although the ejector has a simple structure, there are also quite complex flow mechanisms and phase change condensation phenomena inside, hence, simple numerical optimization simulation research can no longer meet the requirements of industrial production. The research on the condensation characteristics of the ejector is further enriched and diversified in recent years. The phase transition behaviour in the ejector is very complex and changeable, so it is necessary to analyse the phase transition phenomenon occurring in the ejector, to obtain the best parameters and external factors to optimize its performance. In 2015, Ariafar and other researchers [31] considered the traditional steam ejector with the hydrodynamic model of the wet flow cycle established by ANSYS. Yang et al. [32] studied a supersonic ejector by applying a wet gas operating mathematical method and simultaneously analysed its two performances with it and the dry gas model. In addition, in 2019, Zhang et al. [33] believed that the simulation ability of the existing wet gas model could not reach an expected value, so an improved condensation model was proposed to improve the accuracy of the ejector, which was well reflected in the entrainment ratio. Han et al. [34] established a CFD model of condensation in the internal non-equilibrium state of the injector, which is commonly used in fuel cells, to fully study the deep mechanism when the internal phase transition occurs. The final results under a series of simulation conditions show that showed that the entrainment ratio will be underestimated when internal condensation occurred. Therefore, a comprehensive mathematical model considering

condensation should be established to gain a reasonable prediction of the internal performance of the ejector. Nonetheless, at present, the research on the complex phase change phenomenon of ejectors is still limited, and many predictable deep condensation mechanisms need to be explored, especially the analysis of the multi-angle condensation characteristics under different conditions. It is undeniable that mastering the phase change behaviour and entropy generation and transfer during the phase change process will be the key chessman for the ejector to use green energy such as hydrogen energy for efficient utilization.

According to the summary, the research focusing on the internal phase transition of the ejector capable of recirculating residual unreacted hydrogen in the PEMFC system is deficient, especially the energy analysis. Therefore, the focus of this paper is to analyse the phase change and energy change characteristics of the ejector under different conditions. Based on classical nucleation and droplet growth theory, a CFD model combined with the non-equilibrium condensation and entropy transport equations was established to simulate condensation behaviour in the primary and secondary flows for the ejector. Compared with the experimental results of the Laval nozzle and the ejector established in this study, the reliability of the physical structure and mathematical model was fully validated. The phase change and its effects on the internal certain specific characteristics of the ejector were analysed. Finally, the entropy generation and exergy distribution inside the ejector were explored under the dry gas and wet gas models. Substantially, the contribution of this paper is to promote the in-depth development of this field and achieve a win–win balance between energy utilization and environmental governance.

2. Ejector-driven hydrogen recirculation system

The working principle of the hydrogen recirculation system driven by the traditional ejector is shown in Fig. 1. The dry hydrogen stored in the high-pressure tank is delivered to the main nozzle of the ejector after the pressure-reducing link regulated by the pressure regulator, which is called the primary flow. Subsequently, due to the acceleration and pressure drop process in the nozzle, the primary flow will form a low-pressure zone at the nozzle outlet, improving its entrainment capacity of the unreacted hydrogen and water vapour from the anode outlet, which is called the secondary flow. Then the two will be mixed in the mixing chamber. Finally, the mixed flow passes through the last part of the ejector, namely the diffuser, and then enters the anode inlet and is delivered to the fuel cell stack. What must be noted in this process is that excess liquid water may cause the fuel cell to be wet [35], which will damage the internal stability of the fuel cell and adversely affect its performance [36], and even destroy the stability of the internal structure of the fuel cell. Therefore, it is necessary to separate the liquid water generated in the reaction process from the gas–liquid separator in time. Since liquid water is constantly accumulating in the separator, it is necessary to discharge the liquid water regularly with a cleaning valve.

In this hydrogen recirculation system, it is undeniable that the role played by the ejector is enormous. As shown in Fig. 2, the traditional ejector is mainly composed of the main convergence nozzle, suction chamber, mixing chamber, constant area section and diffuser, without

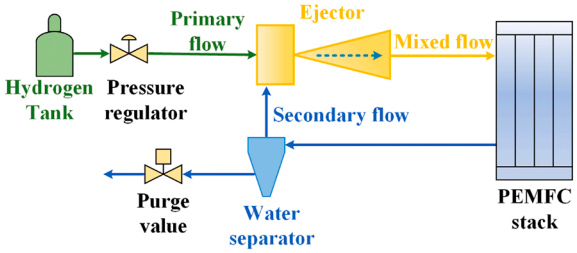

Fig. 1. Process flow diagram of the overall fuel cell system.

moving parts. If the ejector can be operated under high-efficiency conditions, the hydrogen supply capacity can be greatly improved. The entrainment ratio E_R used to evaluate the energy efficiency of the ejector is defined as:

$$E_R = \frac{m_s}{m_p} \tag{1}$$

where m_s and m_p represent the secondary and the primary mass flow respectively.

The specific exergy is defined as

$$E_X = h_{in}^* - h_0 - T_0\left(s_{in}^* - s_0\right) \tag{2}$$

where h_{in}^* represents the total enthalpy, T_0 represents the reference environment temperature, and h_0 is the enthalpy at T_0. Equally, s_{in}^* represents the entropy, s_0 is the entropy at T_0. E_D is calculated by

$$E_D = T_0 s_{gen} = T_0\left(s_c - \frac{1}{1+E_R}s_p - \frac{E_R}{1+E_R}s_s\right) \tag{3}$$

where s_{gen} is entropy generation, s_{c}, s_{p}, and s_{s} can be described as exit entropy, the primary entropy and the secondary entropy of ejector respectively.

Exergy destruction ratio ζ_D is calculated by the formula as

$$\zeta_D = \frac{(1+E_R)E_D}{E_{X,p} + E_R E_{X,s}} \tag{4}$$

where $E_{X,p}$ and $E_{X,s}$ are defined as the exergy energy in the exit of primary and secondary respectively.

3. Mathematical model

3.1. Wet hydrogen flow conservation equations

In previous studies, there were many mathematical models for solving the process of mutual transformation between gas and liquid in supersonic flows. It is not laborious to conclude that it is an effective method to analyse condensation from a non-equilibrium state to an equilibrium state to deal with such problems [37-40].

The gas phase was simulated using compressible gas flow and a multi-species transport model (i.e., hydrogen and water vapour). The interaction was completed by adding source term equations. In addition, high-speed compressible flow occurs inside the ejector, which will produce complex phenomena. The continuity equations of each conservation are described as follows,

$$\frac{\partial \rho}{\partial t} + \nabla \bullet (\rho \overline{u}) = S_m \tag{5}$$

In this formula, u is the velocity. ρ is the density. And we can see that the S_m represents the mass source term.

$$\frac{\partial(\rho \overline{u})}{\partial t} + \nabla \bullet \left(\rho \overline{u_i u_j}\right) = -\nabla \bullet p + \nabla \bullet (\overline{\overline{\tau}}) + S_F \tag{6}$$

Similarly, $\overline{\overline{\tau}}$ is the stress tensor. S_F describes momentum source term.

$$\frac{\partial(\rho E)}{\partial t} + \nabla \bullet [\overline{u}(\rho E + p)] = -\nabla \bullet \left(\lambda \bullet \nabla T - \sum_j h_j J_j + \overline{\overline{\tau}} \bullet \overline{u}\right) + S_h \tag{7}$$

In this formula, p is the pressure. E is the energy. S_h represents the conservation of energy in the continuity equation. hj is the enthalpy.

And the species transfer equation of hydrogen and water vapour involved in the ejector is

$$\frac{\partial(\rho Y_j)}{\partial t} + \nabla \bullet (\rho \overline{u} Y_j) = -\nabla \bullet \overline{D}_j \tag{8}$$

The three source terms mentioned above are defined by the following

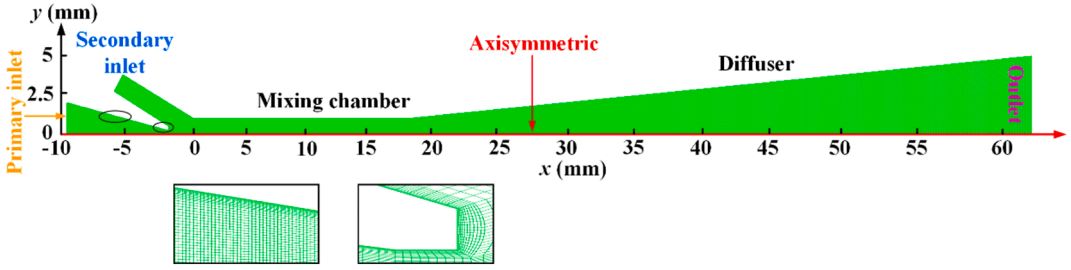

Fig. 2. Geometry and mesh generation for hydrogen recirculation ejector.

formula.

$$S_m = -m_v \tag{9}$$

$$S_F = -m_v u \tag{10}$$

$$S_h = m_v(h - h_{lg}) \tag{11}$$

In the above formula, m_v can be defined as the mass generation rate, h is enthalpy and h_{lg} represents the latent heat.

For the liquid phase, part of the established mathematical model, the Y and N (m^{-3}) represent the liquid mass fraction and droplet number. We can describe the Y and N using the formula as follows,

$$\frac{\partial(\rho_m Y)}{\partial t} + \nabla \bullet (\rho_m \bar{u} Y) = m_v \tag{12}$$

$$\frac{\partial(\rho N)}{\partial t} + \nabla \bullet (\rho \bar{u} N) = \rho I \tag{13}$$

where ρ_m is the density of the mixture. I ($m^{-3}{\cdot}s^{-1}$) represents the nucleation rate.

3.2. The nucleation and droplet growth model

According to previous theories, the overall condensation process for wet gas includes nucleation and droplet growth process. In addition, water vapour will not condense immediately when it reaches saturation but will only condense at a place where it needs to reach supersaturation, i.e., Wilson's point. At this time, with the sudden formation of many small droplets, the supersaturated steam will be in a non-equilibrium state. After that, these droplets continue to grow until the process ends and the equilibrium state is restored. It can be seen from the above description that the mass generation rate m_v consists of nucleation and droplet growth. The specific description is as follows

$$m_v = \frac{4}{3}\pi\rho_l I r_c^3 + 4\pi\rho_l N r^2 \frac{\partial r}{\partial t} \tag{14}$$

The ρ_l is the density in the liquid phase. r is used as the description for droplet radius (m).

In addition, r_c (m) is the critical radius, as given by

$$r_c = \frac{2\sigma}{\rho_l R T \ln S} \tag{15}$$

We can see that S is the degree of supersaturation. R represents the gas constant.

The σ is the surface tension which is defined as

$$\sigma = 85.27 + 75.67 \times \frac{T_g}{647.3} - 256.889 \times \left(\frac{T_g}{647.3}\right)^2 + 95.928 \times \left(\frac{T_g}{647.3}\right)^3 \tag{16}$$

The modified nucleation rate [41] is defined as [42]

$$I = \frac{q_c}{1+\theta}\frac{\rho_v^2}{\rho_l}\sqrt{\frac{2\sigma}{\pi M_m^3}}\exp\left(-\frac{4\pi\sigma r_c^2}{3k_B T}\right) \tag{17}$$

where q_c is the condensation factor and ρ_v is the density of the vapour. k_B is Boltzmann's constant, and its value is fixed, equal to 1.38×10^{-23} $J{\cdot}K^{-1}$. M_m is the water molecular mass. θ is a non-isothermal correction factor. θ can be written as

$$\theta = \frac{2(\gamma-1)}{\gamma+1}\frac{h_{lg}}{RT}\left(\frac{h_{lg}}{RT} - \frac{1}{2}\right) \tag{18}$$

Apart from the nucleation behaviour, droplet growth is an important process reflecting gas–liquid two-phase transfer. The modified formula of droplet growth rate [43] is as follows

$$\frac{dr}{dt} = \frac{\lambda(T_s - T)\left(1 - \frac{r_c}{r}\right)}{\rho_l h_{lg} r\left(\frac{1}{1+2\beta Kn} + 3.78(1-v_0)\frac{Kn}{Pr}\right)} \tag{19}$$

where λ is thermal conductivity, T_s is the saturation temperature. β is a correction factor, Kn is the Knudsen number, and Pr is the Prandtl number. The correction factor v_0 can be calculated by

$$v_0 = \frac{RT_s}{h_{lg}}\left(\alpha - 0.5 - \frac{2-q_c}{2q_c}\frac{\gamma+1}{2\gamma}\frac{c_p T_s}{h_{lg}}\right) \tag{20}$$

where $\alpha = 9$.

3.3. Selection of turbulence model, SST k-ω

SST k- ω has more advantages in the complex flow of the ejector under the premise of comprehensive consideration of calculation cost. This is another important mathematical model besides the mathematical description of phase change condensation. According to the existing theoretical manual, the turbulent kinetic energy k, and the specific dissipation rate are calculated using the following formulas [44]:

$$\frac{\partial}{\partial t}(\rho k) + \frac{\partial}{\partial x_i}(\rho k u_i) = \frac{\partial}{\partial x_j}\left(\Gamma_k \frac{\partial k}{\partial x_j}\right) + \overline{G_k} - Y_k + S_k \tag{21}$$

$$\frac{\partial}{\partial t}(\rho\omega) + \frac{\partial}{\partial x_i}(\rho\omega u_j) = \frac{\partial}{\partial x_j}\left(\Gamma_\omega \frac{\partial k}{\partial x_j}\right) + \overline{G_\omega} - Y_\omega + D_\omega + S_\omega \tag{22}$$

3.4. Entropy generation terms

In this study, we also need to analyse the entropy generation, and the entropy s of the internal ejector is defined as

$$s = \beta s_l + (1-\beta)s_g \tag{23}$$

The total entropy generation can be mainly composed of the following four parts, and the calculation formula can be expressed as

$$s_{gen} = s_{gen,D} + s_{gen,C} + s_{gen,L} + s_{gen,A} \tag{24}$$

Global entropy consists of four parts, $s_{gen,D}$, $s_{gen,C}$, $s_{gen,L}$ and $s_{gen,A}$. To facilitate understanding and calculation, viscous dissipation and convective heat transfer will be divided into two independent parts in the mathematical expression, namely $s_{gen,D} = s_{gen,D} + s_{gen,D'}$ and $s_{gen,C} = s_{gen,C} + s_{gen,C'}$. The entropy generation distribution satisfies the

superposition principle [45], thus each part of entropy generation is expressed as

$$\frac{\partial}{\partial t}(\rho s_{\varnothing}) + \frac{\partial}{\partial x_i}(\rho s_{\varnothing}\overline{u}_i) = Y_{\varnothing} \tag{25}$$

$$Y_{Gen,\overline{D}} = \frac{2\mu S_{i,j}S_{i,j}}{T} \tag{26}$$

$$Y_{Gen,D'} = \frac{\rho\beta^* k\omega}{T}, \beta = 0.09 \tag{27}$$

$$Y_{Gen,\overline{C}} = \frac{\lambda}{T^2}\frac{\partial T}{\partial x_i}\frac{\partial T}{\partial x_i} \tag{28}$$

$$Y_{Gen,C'} = \frac{\alpha_t}{\alpha}Y_{Gen,C'} = \frac{\alpha_t}{\alpha}\frac{\lambda}{T^2}\frac{\partial T}{\partial x_i}\frac{\partial T}{\partial x_i} \tag{29}$$

where α_t is turbulent thermal diffusivity.

$$Y_{Gen,L} = m_v h_{lg}\left(\frac{1}{T} - \frac{1}{T_l}\right) \tag{30}$$

The source term of the energy transfer equation is:

$$Y_{tran} = \frac{\partial}{\partial x_i}\left(\frac{\lambda_{eff}}{T}\frac{\partial T}{\partial x_i}\right) \tag{31}$$

4. CFD validation

4.1. Numerical calculation

4.1.1. Explanation of numerical scheme

In this study, the control equations of the gas and liquid phase were discretized by the finite volume method. A density-based solver with the implicit solution formulation and axis-symmetric model is used to obtain a stable solution of convergence faster. The spatial discretization of the convective term adopts the first-order upwind scheme, and the diffusion term adopts the central difference method. The boundary conditions of the inlet and outlet are the pressure inlet and pressure outlet states, respectively. The structured grid discretization method is adopted in CFD simulation to effectively reduce numerical divergence. In addition, in the numerical calculation process, the SST k-ω turbulence model [46] is selected to predict the shock wave phenomenon because of its high accuracy in predicting the condensation behaviour of the ejector flow, which is also mentioned in the mathematical model section. Furthermore, the model is assumed to be a two-dimensional axisymmetric flow and the fluid is assumed to conform to the ideal gas equation of state, ignoring the influence of gravity in the simulation process.

What's more, the UDS and UDM are used to calculate phase transition behaviour in wet steam flow [47-49], mainly there are equation variables and key parameters of condensation [50,51].

4.1.2. Grid independence verification

For reducing the calculation expense and improving calculation speed, a two-dimensional axisymmetric grid is used for this calculation, which can be seen in Fig. 2 for details. To ensure that the divided grids of the ejector can not only ensure the prediction ability of the wet hydrogen mathematical model but also effectively save the calculation cost and space, this study uses the grid convergence index (GCI) [52] to evaluate the grid independence. GCI is an estimation method with high accuracy that depends on mathematical error analysis. A common calculation method of GCI is

$$GCI = \frac{F_s|\varepsilon|}{r^p - 1} \times 100\% \tag{32}$$

In this formula, F_s is the safety factor. ε is the relative error of different grids, and r is the ratio of the refinement factor. And it can be found that p represents the order of the algorithm.

In this verification process, three grids with different refinement levels were constructed for validation: 1: fine grid (85200 structural grids), 2: medium grid (74495 structural grids), and 3: coarse grid (57900 structural grids). The final results are shown in the following table in Table 1. According to the calculation results, it is not difficult to find that the increase in the number of grids cannot effectively improve the accuracy of the computational domain, that is, the performance in the ejector will not have obvious incalculable consequences due to the extremely refined grid. It can be seen that the GCI results of 1 and 2 can both meet the calculation accuracy requirements. Therefore, 74,495 moderately refined grids are used for further research, which can balance the relationship between calculation accuracy and calculation cost to a certain extent.

4.2. Validation by supersonic nozzle

As for the validation part of experimental data: The validation was performed in a 3D toroidal-throat supersonic nozzle with a throat diameter d of 10 mm and a curvature radius of 870 mm in our experiment. The size and grid structure of the supersonic nozzle used for this validation are shown in Fig. 3. In the validation process, the working fluid was wet air, and the boundary conditions used in the simulation were set to be 3 atm for the inlet pressure and 1 atm for the outlet pressure. Consistent with the method mentioned in section 4.1, the grid independence verification was similarly conducted to guarantee the fastest computation speed and relatively low computation cost. The pressure distribution around the nozzle wall with different inlet relative humidity Φ^{in} was given in Fig. 4, respectively. The simulation results of computational fluid mechanics fit well with the experimental results, that is, the model we established in this study can effectively simulate and predict the gas–liquid relationship evolution behaviour of the convergent nozzle and its outlet of the ejector.

4.3. Validation by hydrogen recirculation ejector

In this study, the experimental data of K. Nikiforow [53] was extracted to further verify the usefulness of the wet gas model inside the ejector. According to the data provided in K. Nikiforow's experiment, the ejector geometrical sizes used in this validation was shown in Table 2. The two-dimensional axisymmetric calculation area and mesh generation of the ejector were shown in Fig. 2. To guarantee the calculation accuracy, the grids of the ejector's wall and throat were refined. According to the experimental data, four groups of simulation cases are selected for this validation, that is, the pressure (bar) of primary flow $p_{p,\,in}$ is 3.0, 4.0, 5.0 and 6.0 respectively, while the pressure of secondary flow $p_{s,\,in}$ and the pressure of outlet p_{out} remain unchanged at 1.2 bar and 1.25 bar. It is worth emphasizing that, according to the calculation results, there is no obvious difference in the mass flow rate of primary flow under the experimental data, dry gas model and wet gas model. For example, when the inlet pressure varies from 3.0 to 6.0 bar, the primary mass flow rates of the dry gas model and wet gas model are consistent, and the difference between them and experimental data is kept within 1.6×10^{-6} kg/s. For example, when the inlet pressure is 3.0 bar, the primary mass flow rate of the wet gas model, dry gas model and experimental data are 3.34×10^{-5}, 3.34×10^{-5} and 3.42×10^{-5} kg/s respectively. When the pressure rises to 6.0 bar, the value of mass flow

Table 1
The numerical outcome of grid independence verification.

		Grids 1–2 (1-Superior, 2-moderate)		Grids 2–3 (2-Moderate, 3-inferior)	
F_s	p	$\varepsilon_{1,2}$(%)	$GCI_{1,2}$(%)	$\varepsilon_{2,3}$(%)	$GCI_{2,3}$(%)
3	3	0.16	0.77	0.63	2.31

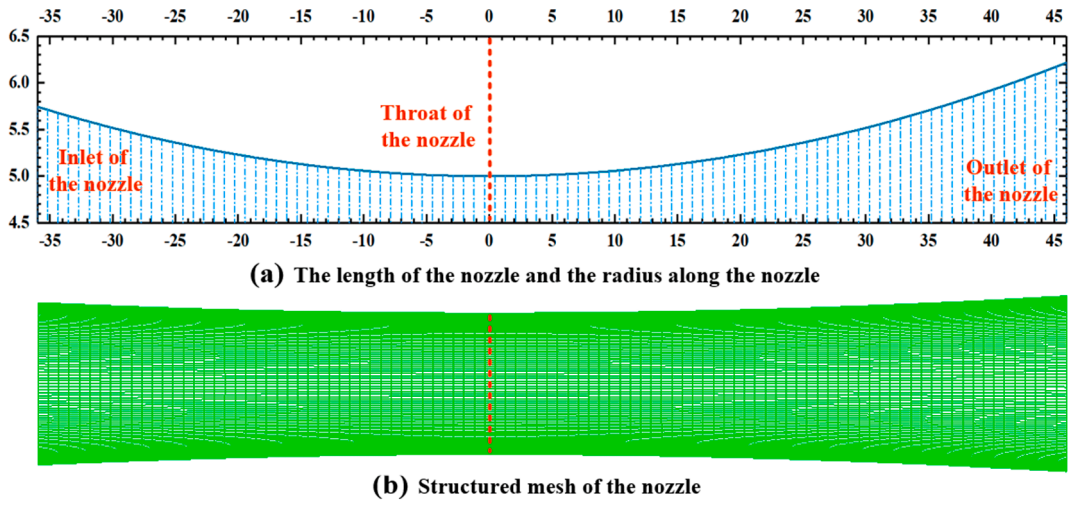

Fig. 3. Dimensions and grids refinement of the supersonic nozzle.

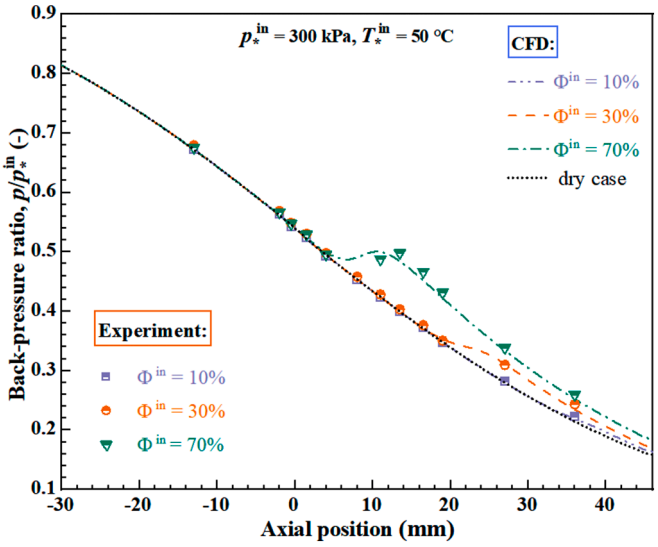

Fig. 4. Comparison of axial pressure of CFD with experiment data under different inlet relative humidity.

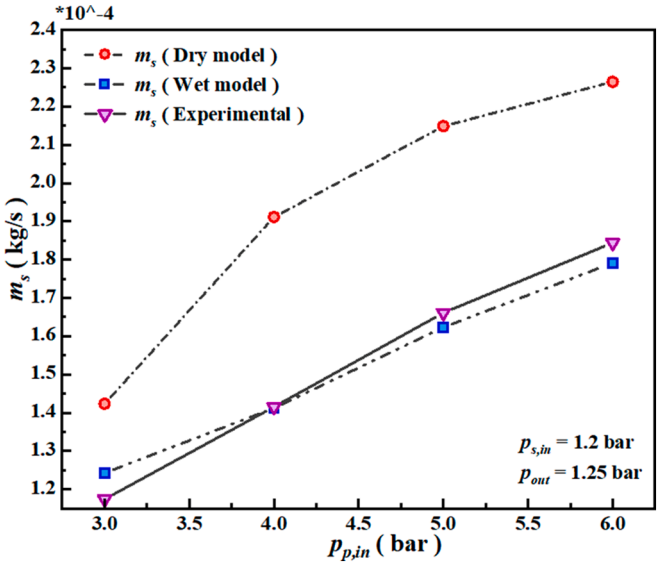

Fig. 5. Comparison of the results of secondary mass flow rate between dry and wet gas models.

Table 2
Dimension parameters for each part of the ejector.

Geometrical sizes	Dimensions (mm)
Primary inlet diameter	4
Converging length of primary inlet	7.5
Secondary inlet diameter	2.104
Mixing chamber outlet diameter	2
Length of the mixing chamber	1.8
Constant area zone diameter	2
Length of the constant area	16
Diffuser diameter	10
Diffuser length	45.72

rate is 6.79 × 10^{-5}, 6.79 × 10^{-5} and 6.94 × 10^{-5} kg/s respectively. The comparison of the secondary mass flow rate between the simulation results of the dry gas model, the wet gas model, and the experimental results is shown in Fig. 5. The difference in secondary mass flow rate between the dry gas model and the wet gas model is quite significant. And the secondary mass flow rate of the dry gas is generally larger than that of the wet gas model. The reason is that, compared with the dry gas model, the wet gas model has phase change condensation. However, the condensation process will release some latent heat, which will inevitably affect the heat and mass transfer behaviour in the flow process, and then lead to great differences in the characteristics of various parameters.

To achieve a more convincing explanation of the accuracy of the experimental data, ***MRE***, which is defined as average relative errors between the two arbitrary results, is used as an evaluation index to obtain the difference between the dry and wet gas models and the experimental data, as shown in Fig. 6. The *MRE* can be calculated using the following formula,

$$MRE = \frac{1}{n}\sum_{i=1}^{n}\left|\frac{(y_i - \overline{y_i})}{y_i}\right| \tag{33}$$

In the above formula, $\overline{y_i}$ is the simulation result, y_i is the real result obtained by the experiment, and n is the amount of the total data. It shows that the *MRE* between the dry gas and the experimental data is far greater. The *MRE* between the dry gas model and the experimental data is 30.17%, while that between the wet gas model and the experimental data is only 2.53%. That is, the wet gas flow model has more superiorities when it is used to predict the condensation behaviour in the hydrogen recirculation ejector, with higher prediction ability and

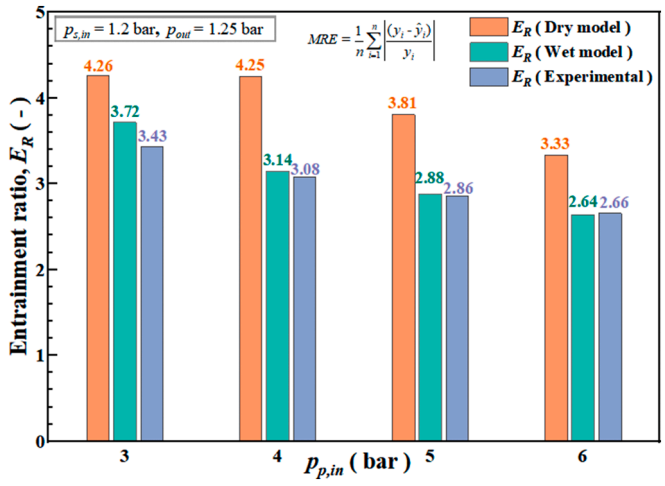

Fig. 6. Relative error of entrainment rate E_R between dry and wet gas models relative to experimental results.

accuracy. At the same time, it can also be concluded that the mathematical model established in this study can be used to simulate the entrainment performance of the ejector.

5. Results and discussion

5.1. Differences in ejector between dry gas and wet gas models

In the validation section above, there are obvious differences between the dry gas model and the wet gas model in predicting the entrainment ratio, but there are also other important parameters in the hydrogen recirculation ejector that need to be explored. Therefore, the different performances of the ejector under the dry and wet gas models will be analysed from multiple angles under the same inlet conditions and different inlet conditions. Firstly, the Mach number, pressure, and temperature of the two models will be investigated under the typical conditions that the inlet pressure for primary flow is 4 bar, the inlet pressure for secondary flow and the pressure of outlet are 1.20 and 1.250. The specific results are shown in Fig. 7.

According to Fig. 7, it could be found that the performance of the dry and wet gas conditions in the ejector's primary nozzle is basically in good agreement with the Mach number, pressure and temperature, while they all show oscillation type changes in the mixing chamber. However, in the mixing chamber and constant area section, it is obvious

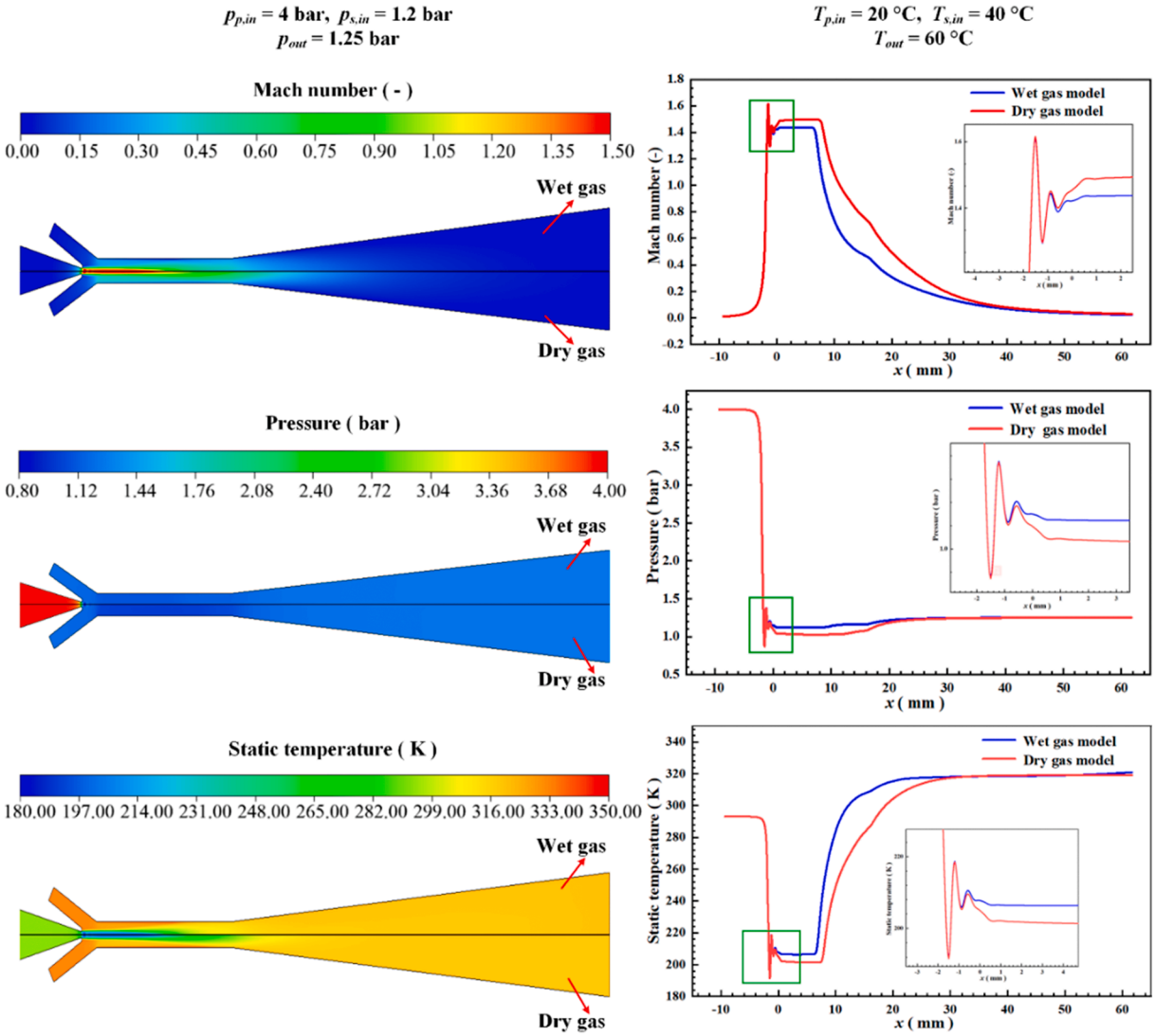

Fig. 7. Comparisons of Mach number, pressure and temperature between dry and wet gas at $p_{p,\ in}$ = 4.0 bar with $p_{s,\ in}$ = 1.2 bar p_{out} = 1.25 bar.

that the speed in the dry gas working condition inside the injector will be higher than that in the wet gas working condition. This is because condensation is taken into account in wet-gas model simulations. When the droplets are generated, part of the energy in the gas phase is obtained by the droplet and becomes the energy of the droplet itself, so the gas phase speed will be reduced when the droplet is generated. So, compared with the wet gas model, the dry gas model overestimates the expansion process of the ejector, and its Mach number is higher. In addition, there is a significant difference, that is the temperature in wet gas conditions is higher, between the two model's results according to the temperature distribution of the axis of the ejector. Because a large amount of latent heat will be released when the droplets are generated, then the mixed flow is secondarily heated. Similarly, the pressure is slightly higher in the wet gas model due to the pressure shocks generated by the condensation.

Except for studying the differences in the performance of the two models in the injector under the same conditions, this section also starts from different inlet conditions to elaborate on a significant evaluation, criterion entrainment ratio, which can fully reflect the performance of the ejector. And another extremely informative parameter is the degree of supercooling in the process of condensation. As can be seen from Fig. 8, the result of the entrainment rate simulated by dry gas working conditions is significantly higher. The dry gas model is known to have lower pressures than the wet steam flows, and lower pressure means a lower differential pressure, which makes the secondary flow easier to entrain, resulting in a higher entrainment ratio. It is also obvious that the entrainment ratio both rises first and then it will show an overall downward trend with the rise of primary flow pressure. This is because, with the rise of the primary flow pressure, the velocity at the nozzle exit increases continuously, and finally reaches supersonic speed. Finally, a low-pressure area will be formed at the nozzle exit, which makes the entrained ability of the secondary inlet increase. Subsequently, as the primary flow pressure continues to increase, the entrainment ratio will decrease on the contrary. Due to the high inlet pressure of the primary flow, it is impossible to form an ideal low-pressure area at the nozzle outlet when the flow passes through the nozzle convergence section, which will reduce the expected entrainment performance of traditional injectors. For example, as shown in Fig. 8, the entrainment ratio under the dry gas model is about 4.26 when the simulation condition of primary flow is set manually, the inlet pressure is 3.0 bar, while that of the wet flows under this condition is about 3.72. When the inlet pressure condition is normally set to 4.0 bar, the entrainment ratio under the dry gas condition reaches 4.25, which is about 1.11 greater than that of the wet gas. Again, when the inlet pressure condition is normally set to 5.0 bar, the entrainment ratio simulated by the dry gas model is 3.81, while that obtained by the wet gas model is only 2.88. In summary, compared with the wet gas condition, the dry gas condition significantly overestimates the entrainment performance of the injector. It is worth mentioning that the reason why the entrainment rate is consistent before 2.5 bar is that there is no obvious phase change condensation behaviour before that, and there is no phase change influence between dry gas and wet gas models.

Fig. 9 shows the degree of supercooling distribution along the ejector centre under the operating conditions of dry and wet gas respectively with the pressure of the primary flow being 3.0, 4.0, and 5.0 bar. Under identical pressure conditions, the maximum degree of supercooling with the dry gas model is somewhat larger than the wet gas working condition. At the same time, the difference between the two conditions will increase as the primary inlet pressure is set higher. Moreover, the location of the maximum supercooling, that is, the Wilson point, occurs in the constant area section of the ejector. Because the point with the degree of supercooling of 0 K is defined as the saturation point, it can be seen in Fig. 9 that the greater the inlet pressure, the easier it is to reach the saturation state, that is, the saturation point appears more forward. For example, as the inlet pressure condition is artificially set to 5 bar, the degree of supercooling in the mixing chamber increases to 0 K at −0.54 mm, and when inlet pressure is 3.0 bar and 4.0 bar respectively, the saturation position appears in the constant section, where the axial position is 5.37 mm and 1.44 mm.

5.2. Phase change characteristics in the ejector based on the wet gas model

From the discussion and analysis in sections 4.3 and 5.1, the wet gas operation condition performs better in its working process of predicting the internal working mechanism of the ejector and has higher prediction accuracy and advantages. In addition, the underlying reasons for the significant differences between the wet and dry gas models can be further explained by the complex flow mechanism. Therefore, according to the previous analysis, under the condition of wet gas, the phase change characteristics inside the injectors will be studied from the perspective of non-equilibrium condensation. The pressure magnitude has a significant effect on the non-equilibrium condensation characteristics in the ejector. Fig. 10 presents the change principle in the location of Wilson point where is the occurrence of condensation of the wet gas model under different primary flow inlet pressure conditions. The Wilson point position is more posterior as the primary pressure increases. For example, condensation occurs at 6.26 mm as the pressure of primary flow reaches 3.0 bar, while the Wilson point position is 6.92 mm and 7.86 mm respectively when the pressure (bar) of primary flow is increased from 4.0 to 5.0. So, there is a larger pressure difference between primary and secondary flow will cause the condensation position to be more posterior in the ejector.

It can be seen from Fig. 11, the contour distribution of nucleation rate and droplet growth rate under the wet gas condition at primary flow

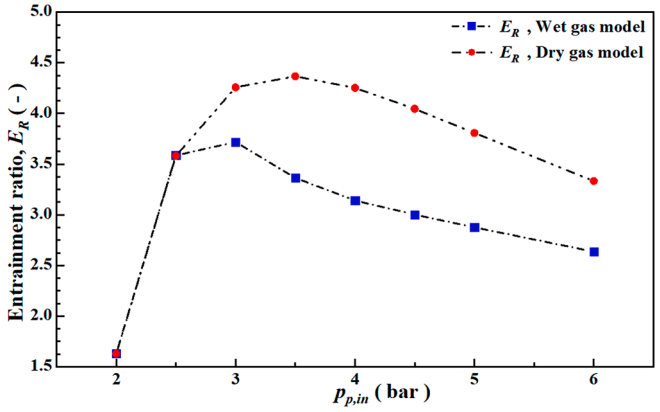

Fig. 8. The changing trend of entrainment rate under different inlet pressure.

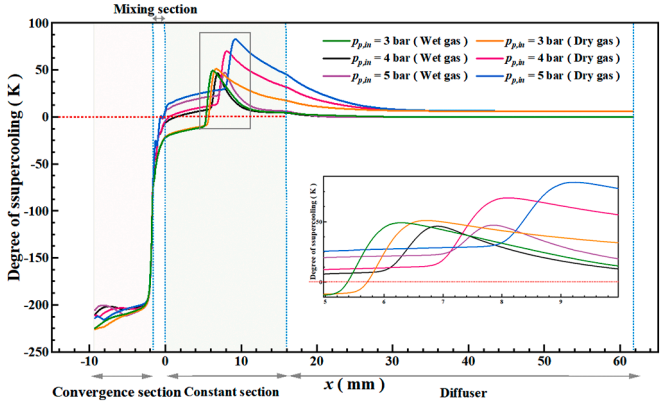

Fig. 9. The difference in the degree of supercooling distribution between the dry and wet gas conditions at different inlet pressures.

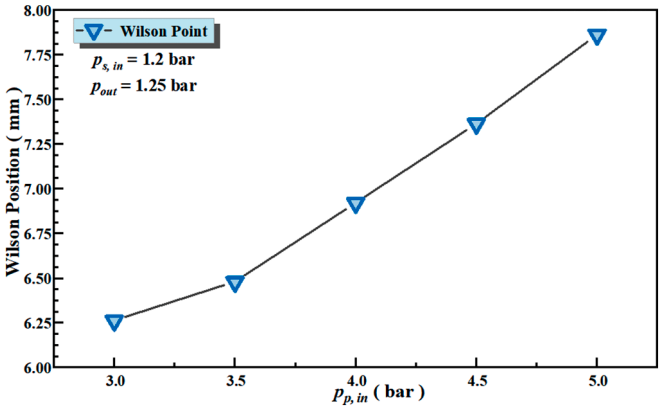

Fig. 10. Condensation location (Wilson point) distribution at different inlet pressures.

inlet pressures of 3.0, 4.0, and 5.0. The droplet nucleation intensity will increase as the inlet pressure is amplified. Moreover, the same information given in Fig. 11 is that more region with the largest nucleation rate is concentrated near the mixing chamber. For the droplet growth rate, it increased when the inlet pressure is set to a larger value and the maximum droplet growth rate can reach 1.2 mm/s when the primary inlet pressure is set to 5.0, while as the inlet pressure is reduced to 3.0, the maximum of droplet growth rate is only 0.78 mm/s. As can be similarly seen through contour plot profiles, the droplet growth rate is closely related to the droplet nucleation rate, and the larger the pressure at the primary flow inlet, the location of the largest droplet growth rate will be advanced.

It is worth noting that another important parameter reflecting the condensation strength is the liquid phase fraction at the exit, which is significantly amplified with the rise of the primary pressure. As shown in Fig. 12, when the primary pressure is less than 2.5 bar, there is almost no condensation phenomenon inside the ejector under the wet gas condition and the liquid phase fraction is zero. With the rise of the primary pressure, the liquid phase fraction Y_{out} at the exit will enhance subsequently, and it can reach 4.56 % when the operating condition with inlet pressure is 3.0 bar and then increases to about 15.35% when that pressure rises to 5.0 bar.

5.3. Entropy and exergy analysis

Based on a series of analyses and summaries, starting from the mechanism of energy, this study aims to improve the performance of the ejector from multiple perspectives. We certainly require analyzing the generation of total entropy and the exergy energy. First, entropy generation and its composition have been introduced in the section of a mathematical model, and the composition of the four terms of entropy generation is known. These four aspects include viscosity loss, convective heat transfer, phase change and aerodynamic loss. They exist in different regions, and of course, there are obvious differences in numerical values. According to the complexity and capricious of entropy distribution contribution, we calculated the entropy generation based on the difference between dry and wet gas. The distribution of entropy at different inlet pressures in the wet model is shown in Fig. 13, of which viscous loss entropy production $s_{gen,\,D}$ is the plate with the largest value in the entropy generation composed of four proportions, followed by aerodynamic loss entropy production $s_{gen,\,D}$. To observe the entropy

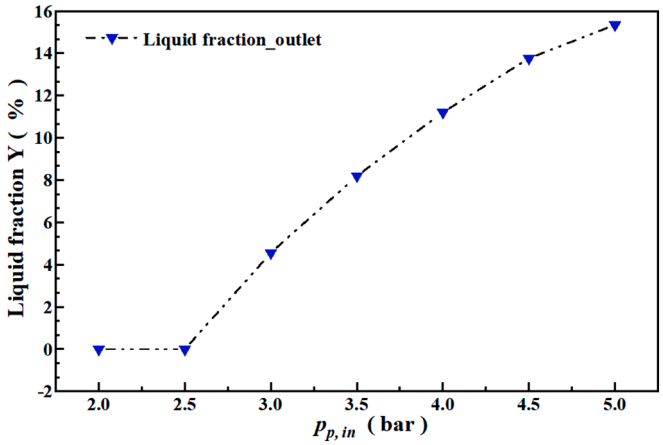

Fig. 12. Liquid phase mass fraction profiles of the outlet under different inlet pressures.

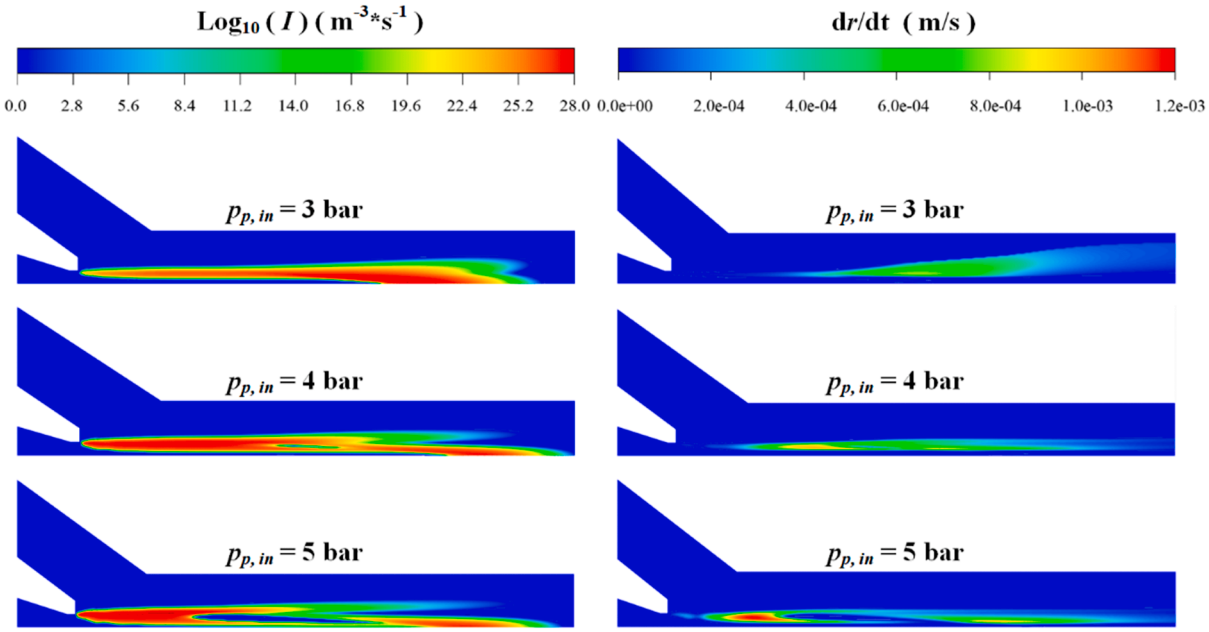

Fig. 11. Distribution of nucleation rate and droplet growth rate under different inlet pressures.

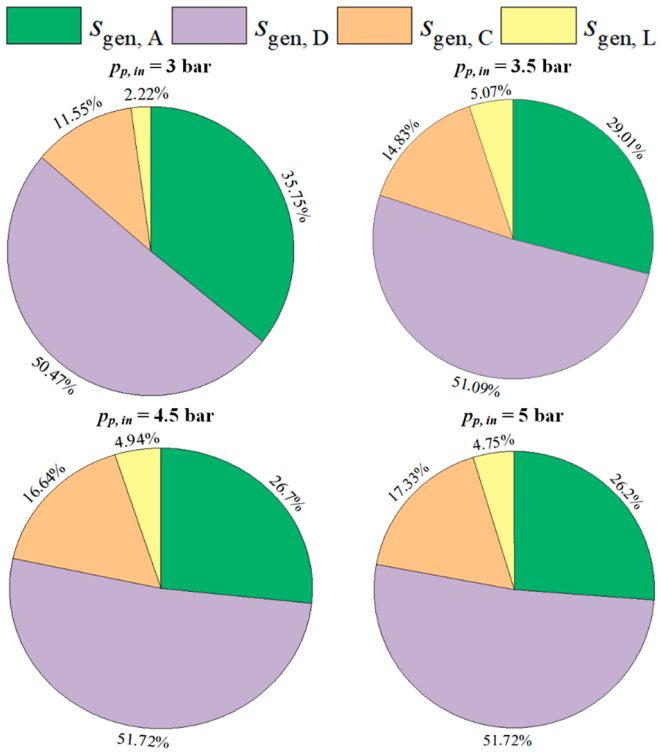

Fig. 13. The Pie chart of four components of entropy generation under wet gas conditions.

generation value of each part more intuitively, Table 3 gives the simulation data of the entropy of the wet gas model. When the inlet pressure is 3 bar, viscous loss entropy $s_{gen,\ D}$ is about 50.74%, convective heat transfer entropy $s_{gen,\ C}$ is about 14.55%, phase change entropy $s_{gen,\ L}$ is 2.22%. And when the inlet pressure is increased to 3.5 bar, viscous loss entropy $s_{gen,\ D}$ increases slightly, rising to 51.09%, moreover, $s_{gen,\ C}$ and $s_{gen,\ L}$ also both increase, which are 14.83% and 5.07%, respectively. When pressure is set to 4.5, the same change laws mentioned above are roughly consistent, that is, $s_{gen,\ D}$ and $s_{gen,\ C}$ increases, however, $s_{gen,\ L}$ slightly declines. It can be noticed that with the raise of primary pressure, the aerodynamic loss entropy production $s_{gen,\ D}$ decreases gradually.

To compare the entropy generation distribution of wet gas and dry gas, Fig. 14 gives the entropy value for the above two models under different pressures, it can be seen that the value of entropy production obtained using dry gas condition is generally greater, and as the inlet pressure increases, the gap between the two entropy generation increases, for example, if the pressure gets to 3.0 bar, the dry gas model overestimates the entropy generation with 41.24 J $kg^{-1}K^{-1}$, moreover, if the pressure gets to 5.0 bar, the entropy generation overestimated by the dry gas condition has reached 138.66 J $kg^{-1}K^{-1}$.

As shown in Fig. 15, the exergy destruction E_D and exergy destruction ratio ζ_D of the two models are directly compared. The comparison results indicate that the E_D and ζ_D will increase under different conditions. For wet gas conditions, as inlet pressure increases, the E_D increases from

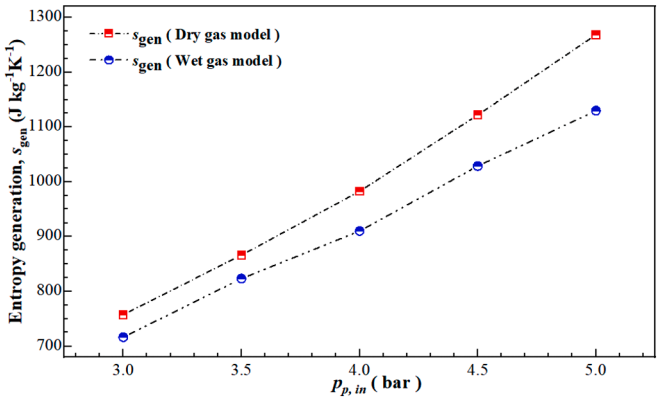

Fig. 14. The entropy generation of the ejector of two mathematical models under different inlet pressures.

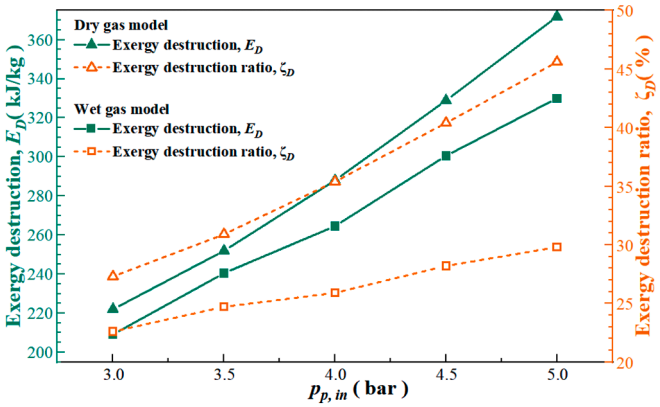

Fig. 15. The exergy destruction E_D and exergy destruction ratio ζ_D with different inlet pressures under dry and wet gas conditions.

209.12 kJ/kg to 330.03 kJ/kg, and the ζ_D increased from 22.66% to 29.80%. In addition, the dry gas model overestimated the E_D and ζ_D when the ejector was working. Similarly, when the inlet pressure increased, the E_D of the dry gas model increased from 222.05 kJ/kg to 371.86 kJ/kg, and the ζ_D increased from 27.29% to 45.63%. According to the calculation, the maximum of E_D and ζ_D overestimated by dry gas can reach 41.83 kJ/kg and 15.83% respectively. The simulation data of exergy can be seen in Table 4.

6. Conclusion

Compared with the key components of conventional fuel cells, the hydrogen recirculation ejectors have become a promising hydrogen energy utilization component because of their advantages of non-parasitic power, simple structure and strong environmental adaptability. To have a more comprehensive grasp of the injector's working principle, improve its performance, and achieve the maximum internal efficiency of energy utilization, a physical structure and mathematical

Table 3
The entropy generation (J·kg^{-1}·K^{-1}) for the wet gas model at different inlet pressures.

$p_{p, in}$	$s_{gen, A}$	$s_{gen, D}$	$s_{gen, C}$	$s_{gen, L}$	s_{gen}
3	260.85	368.23	84.29	2.85	716.22
3.5	250.71	441.49	128.13	2.91	823.24
4	274.08	475.59	152.96	7.35	909.98
4.5	288.03	557.87	179.48	3.37	1028.76
5	309.62	611.33	204.84	4.02	1129.82

Table 4
The exergy destruction E_D (kJ/kg) and exergy destruction ratio ζ_D with dry and wet gas models.

$p_{p, in}$	E_D (Wet gas)	ζ_D (Wet gas)	E_D (Dry gas)	ζ_D (Dry gas)
3	209.12	22.66%	222.05	27.29%
3.5	240.48	24.66%	251.89	30.93%
4	264.61	25.86%	288.06	35.36%
4.5	300.59	28.19%	328.91	40.36%
5	330.03	29.80%	371.86	45.63%

model of hydrogen recirculation ejector were established considering the control equation of species transport. Subsequently, the condensation characteristics as well as entropy and exergy were also analysed by using the simulation strategy of computational fluid dynamics. The main conclusions obtained by the analysis are listed as:

1. In this study, a predicting model with high prediction accuracy has been established, and the prediction accuracy with the *MRE* for the entrainment rate can reach as low as 2.53% under the wet gas model.
2. Compared with the dry gas model, the wet gas CFD model has greater advantages using the ejector. After analysis, the typical parameters such as Mach number, temperature, pressure and entrainment rate are different from the dry gas model. Among them, it is obvious that the dry gas working condition overestimates the entrainment performance of the ejector. As the primary inlet pressure is set to 4 bar, the entrainment rate of the dry gas model is 4.25, which is a larger value than wet gas with 1.1.
3. When the pressure is set to a greater value, the nucleation intensity and droplet growth rate both increase and the stronger part appeared faster in the mixing chamber. In addition, as the inlet pressure increases, the liquid mass fraction at the outlet will also increase.
4. Entropy generation consists of four parts. This study accurately calculated the entropy production of each part and found that viscous loss entropy production $s_{\text{gen, D}}$ is the largest. Moreover, the dry gas operating condition has a higher prediction of the overall entropy generation. With the rise of the inlet primary pressure, the entropy generation value overestimated by the dry gas model will be larger.
5. Whether it is a dry or wet gas model, E_D and ζ_D both rise with the increase of inlet pressure. And the dry gas model overestimated the E_D and ζ_D. As the primary pressure is set to 5 bar, the value of ζ_D overestimated is 15.83% higher than in wet gas conditions.

More meaningfully, it is expected that there will be more experimental methods and results that can be used as strong support, which can be combined with simulation strategies that can apply more computational models for finding a balance condition between the primary flow and the secondary flow to achieve the highest entrainment performance of the ejector so that we can explore this environmentally friendly energy utilization component at a deeper level.

Conflict of interest

The authors declared that there is no conflict of interest.

Data availability statement

The research data supporting this publication are provided within this paper.

CRediT authorship contribution statement

Hongbing Ding: Conceptualization, Supervision, Writing – original draft, Writing – review & editing, Funding acquisition. **Yuanyuan Dong:** Formal analysis, Investigation, Writing – review & editing. **Yu Zhang:** Formal analysis, Investigation, Writing – review & editing. **Yan Yang:** Methodology, Supervision, Writing – review & editing. **Chuang Wen:** Conceptualization, Methodology, Supervision, Validation, Writing – review & editing.

Declaration of Competing Interest

The authors declare that they have no known competing financial interests or personal relationships that could have appeared to influence the work reported in this paper.

Data availability

Data will be made available on request.

Acknowledgement

This work is supported in part by the National Natural Science Foundation of China under Grant 52276159 and 51876143.

References

[1] Jiao K, Xuan J, Du Q, Bao Z, Xie B, Wang B, et al. Designing the next generation of proton-exchange membrane fuel cells. Nature (London) 2021;595(7867):361–9.
[2] He Y, Zhou Y, Yuan J, Liu Z, Wang Z, Zhang G. Transformation towards a carbon-neutral residential community with hydrogen economy and advanced energy management strategies. Energ Convers Manage 2021;249:114834.
[3] Zhang S, Ocłoń P, Klemeš JJ, Michorczyk P, Pielichowska K, Pielichowski K. Renewable energy systems for building heating, cooling and electricity production with thermal energy storage. Renew Sust Energ Rev 2022;165:112560.
[4] Ding H, Zhang Yu, Dong Y, Wen C, Yang Y. High-pressure supersonic carbon dioxide (CO_2) separation benefiting carbon capture, utilisation and storage (CCUS) technology. Appl Energ 2023;339:120975.
[5] Yue M, Lambert H, Pahon E, Roche R, Jemei S, Hissel D. Hydrogen energy systems: A critical review of technologies, applications, trends and challenges. Renew Sust Energ Rev 2021;146:111180.
[6] Sorrenti I, Harild Rasmussen TB, You S, Wu Q. The role of power-to-X in hybrid renewable energy systems: A comprehensive review. Renew Sust Energ Rev 2022;165:112380.
[7] Samsatli S, Samsatli NJ. The role of renewable hydrogen and inter-seasonal storage in decarbonising heat - Comprehensive optimisation of future renewable energy value chains. Appl Energ 2019;233–234:854–93.
[8] Sezgin B, Devrim Y, Ozturk T, Eroglu I. Hydrogen energy systems for underwater applications. Int J Hydrogen Energ 2022;47(45):19780–96.
[9] Ishaq H, Dincer I. Comparative assessment of renewable energy-based hydrogen production methods. Renew Sust Energ Rev 2021;135:110192.
[10] Gasanzade F, Pfeiffer WT, Witte F, Tuschy I, Bauer S. Subsurface renewable energy storage capacity for hydrogen, methane and compressed air – A performance assessment study from the North German Basin. Renew Sust Energ Rev 2021;149:111422.
[11] Wang G, Yu Yi, Liu H, Gong C, Wen S, Wang X, et al. Progress on design and development of polymer electrolyte membrane fuel cell systems for vehicle applications: A review. Fuel Process Technol 2018;179:203–28.
[12] Wang Y, Ruiz Diaz DF, Chen KS, Wang Z, Adroher XC. Materials, technological status, and fundamentals of PEM fuel cells - A review. Materials today (Kidlington, England) 2020;32:178–203.
[13] Hong Z, Li Qi, Han Y, Shang W, Zhu Y, Chen W. An energy management strategy based on dynamic power factor for fuel cell/battery hybrid locomotive. Int J Hydrogen Energ 2018;43(6):3261–72.
[14] Wang B, Wu K, Xi F, Xuan J, Xie Xu, Wang X, et al. Numerical analysis of operating conditions effects on PEMFC with anode recirculation. Energy (Oxford) 2019;173:844–56.
[15] Rogié B, Ryhl Kærn M, Wen C, Rothuizen E. Numerical optimization of a novel gas-gas ejector for fuelling of hydrogen vehicles. Int J Hydrogen Energ 2020;45(41):21905–19.
[16] Potrč S, Čuček L, Martin M, Kravanja Z. Sustainable renewable energy supply networks optimization – The gradual transition to a renewable energy system within the European Union by 2050. Renew Sust Energ Rev 2021;146:111186.
[17] Jianmei F, Qingqing Z, Tianfang H, Xueyuan P. Dynamics characteristics analysis of the oil-free scroll hydrogen recirculating pump based on multibody dynamics simulation. Int J Hydrogen Energ 2021;46(7):5699–713.
[18] Toghyani S, Afshari E, Baniasadi E. A parametric comparison of three fuel recirculation system in the closed loop fuel supply system of PEM fuel cell. Int J Hydrogen Energ 2019;44(14):7518–30.
[19] Chen L, Xu K, Yang Z, Yan Z, Dong Z. Optimal Design and Operation of Dual-Ejector PEMFC Hydrogen Supply and Circulation System. Energies 2022;15:5427.
[20] Jenssen D, Berger O, Krewer U. Improved PEM fuel cell system operation with cascaded stack and ejector-based recirculation. Appl Energ 2017;195:324–33.
[21] Han J, Feng J, Hou T, Peng X. Performance investigation of a multi-nozzle ejector for proton exchange membrane fuel cell system. Int J Energ Res 2021;45(2):3031–48.
[22] Tashtoush BM, Al-Nimr MA, Khasawneh MA. A comprehensive review of ejector design, performance, and applications. Appl Energ 2019;240:138–72.
[23] Tang Y, Liu Z, Li Y, Shi C, Lv C. A combined pressure regulation technology with multi-optimization of the entrainment passage for performance improvement of the steam ejector in MED-TVC desalination system. Energy (Oxford) 2019;175:46–57.
[24] Xue H, Wang L, Zhang H, Jia L, Ren J. Design and investigation of multi-nozzle ejector for PEMFC hydrogen recirculation. Int J Hydrogen Energ 2020;45(28):14500–16.
[25] Kim M, Sohn Y-J, Cho C-W, Lee W-Y, Kim C-S. Customized design for the ejector to recirculate a humidified hydrogen fuel in a submarine PEMFC. J Power Sources 2008;176(2):529–33.

[26] Maghsoodi A, Afshari E, Ahmadikia H. Optimization of geometric parameters for design a high-performance ejector in the proton exchange membrane fuel cell system using artificial neural network and genetic algorithm. Appl Therm Eng 2014;71(1):410–8.
[27] Hosseinzadeh E, Rokni M, Jabbari M, Mortensen H. Numerical analysis of transport phenomena for designing of ejector in PEM forklift system. Int J Hydrogen Energ 2014;39(12):6664–74.
[28] Yin Y, Fan M, Jiao K, Du Q, Qin Y. Numerical investigation of an ejector for anode recirculation in proton exchange membrane fuel cell system. Energ Convers Manage 2016;126:1106–17.
[29] Liu Z, Liu Z, Jiao K, Yang Z, Zhou X, Du Q. Numerical investigation of ejector transient characteristics for a 130-kW PEMFC system. Int J Energ Res 2020;44(5):3697–710.
[30] Yang Y, Du W, Ma T, Lin W, Cong M, Yang H, et al. Numerical studies on ejector structure optimization and performance prediction based on a novel pressure drop model for proton exchange membrane fuel cell anode. Int J Hydrogen Energ 2020;45(43):23343–52.
[31] Ariafar K, Buttsworth D, Al-Doori G, Malpress R. Effect of mixing on the performance of wet steam ejectors. Energy (Oxford) 2015;93:2030–41.
[32] Yang Y, Zhu X, Yan Y, Ding H, Wen C. Performance of supersonic steam ejectors considering the nonequilibrium condensation phenomenon for efficient energy utilisation. Appl Energ 2019;242:157–67.
[33] Zhang G, Zhang X, Wang D, Jin Z, Qin X. Performance evaluation and operation optimization of the steam ejector based on modified model. Appl Therm Eng 2019;163:114388.
[34] Han J, Feng J, Peng X. Phase change characteristics and their effect on the performance of hydrogen recirculation ejectors for PEMFC systems. Int J Hydrogen Energ 2022;47(2):1144–56.
[35] Du Z, Liu Q, Wang X, Wang L. Performance investigation on a coaxial-nozzle ejector for PEMFC hydrogen recirculation system. Int J Hydrogen Energ 2021;46(76):38026–39.
[36] Chen B, Liu Y, Chen W, Du C, Shen J, Tu Z. Numerical study on purge characteristics and purge strategy for PEMFC hydrogen system based on exhaust hydrogen recirculation. Int J Energ Res 2022;46:11424–42.
[37] Yang Y, Walther JH, Yan Y, Wen C. CFD modeling of condensation process of water vapor in supersonic flows. Appl Therm Eng 2017;115:1357–62.
[38] Dykas S, Wróblewski W. Two-fluid model for prediction of wet steam transonic flow. Int J Heat Mass Tran 2013;60:88–94.
[39] Bodys J, Smolka J, Palacz M, Haida M, Banasiak K. Non-equilibrium approach for the simulation of CO2 expansion in two-phase ejector driven by subcritical motive pressure. Int J Refrig 2020;114:32–46.
[40] Ding H, Zhao Y, Wen C, Wang C, Sun C. Energy efficiency and exergy destruction of supersonic steam ejector based on nonequilibrium condensation model. Appl Therm Eng 2021;189:116704.
[41] Kantrowitz A. Nucleation in Very Rapid Vapor Expansions. J Chem Phys 1951;19(9):1097–100.
[42] Bakhtar F, Young JB, White AJ, Simpson DA. Classical Nucleation Theory and Its Application to Condensing Steam Flow Calculations. Proc Inst Mech Eng C J Mech Eng Sci 2005;219(12):1315–33.
[43] Zhang G, Dykas S, Yang S, Zhang X, Li H, Wang J. Optimization of the primary nozzle based on a modified condensation model in a steam ejector. Appl Therm Eng 2020;171:115090.
[44] Besagni G, Cristiani N, Croci L, Guédon GR, Inzoli F. Computational fluid-dynamics modelling of supersonic ejectors: Screening of modelling approaches, comprehensive validation and assessment of ejector component efficiencies. Appl Therm Eng 2021;186:116431.
[45] Ding H, Li Y, Lakzian E, Wen C, Wang C. Entropy generation and exergy destruction in condensing steam flow through turbine blade with surface roughness. Energ Convers Manage 2019;196:1089–104.
[46] Menter FR. Two-equation eddy-viscosity turbulence models for engineering applications. Aiaa J 1994;32(8):1598–605.
[47] Ding H, Zhang Yu, Yang Y, Wen C. A modified Euler-Lagrange-Euler approach for modelling homogeneous and heterogeneous condensing droplets and films in supersonic flows. Int J Heat Mass Transf 2023;200:123537.
[48] Ding H, Dong Y, Zhang Y, Yang Y, Wen C. A potential strategy of CO_2 separation using supersonic flows contributing to carbon capture and storage. Sep Purif Technol 2022;303:122153.
[49] Ding H, Zhang Yu, Sun C, Yang Y, Wen C. Numerical simulation of supersonic condensation flows using Eulerian-Lagrangian and Eulerian wall film models. Energy 2022;258:124833.
[50] Wen C, Li Bo, Ding H, Akrami M, Zhang H, Yang Y. Thermodynamics analysis of CO2 condensation in supersonic flows for the potential of clean offshore natural gas processing. Appl Energy 2022;310:118523.
[51] Yang Y, Karvounis N, Walther JH, Ding H, Wen C. Effect of area ratio of the primary nozzle on steam ejector performance considering nonequilibrium condensations. Energy 2021;237:121483.
[52] Oberkampf WL, Trucano TG. Verification and validation in computational fluid dynamics. Prog Aerosp Sci 2002;38(3):209–72.
[53] Nikiforow K, Koski P, Karimäki H, Ihonen J, Alopaeus V. Designing a hydrogen gas ejector for 5 kW stationary PEMFC system - CFD-modeling and experimental validation. Int J Hydrogen Energ 2016;41(33):14952–70.